Title: Functional Organization for Color Appearance Mechanisms in Primary Visual Cortex

Authors: Peichao Li[1]†, Anupam K. Garg[1,2,3]†, Li A. Zhang[1], Mohammad S. Rashid[1] and Edward M. Callaway[1,2]*

Affiliations:
[1]The Salk Institute for Biological Studies, La Jolla, California, 92037
[2]Neurosciences Graduate Program, University of California, San Diego, La Jolla, California, 92093
[3]Medical Scientist Training Program, University of California, San Diego, La Jolla, California, 92093

*Correspondence to: callaway@salk.edu.
†These authors contributed equally.

Abstract:

Studies of color perception have led to mechanistic models of how signals from cone-opponent retinal ganglion cells are integrated to generate color appearance. But it is not known where or how these hypothesized mechanisms occur in the brain. Here we show that cone opponent signals transmitted from the retina to primary visual cortex (V1) are integrated through highly organized circuits within V1 to generate the color opponent mechanisms that underlie color appearance. Combining intrinsic signal optical imaging (ISI) and 2-photon calcium imaging (2PCI) at single cell resolution, we demonstrate cone-opponent functional domains (COFDs) that combine L/M cone-opponent and S/L+M cone-opponent signals in precisely the combinations predicted from psychophysical studies of color perception. These give rise to an orderly organization of hue preferences of the neurons within the COFDs and the generation of hue "pinwheels". COFDs occupy regions corresponding to both high and low cytochrome oxidase intensity ("blobs" and "interblobs") but have a bias toward blobs. Thus, neural circuits in the primary visual cortex establish the boundary conditions for color opponency and unique hues.

One Sentence Summary:

Cone-opponent functional domains generate color opponent functional architecture in primary visual cortex.

Main Text:

Color vision has a long history of rigorous psychophysical investigation to develop mechanistic models. This has led to some of the greatest successes in linking neural circuit mechanisms to perceptual phenomena. Psychophysical studies led to 3-stage models (*1-5*) (Fig. 1) that presaged the later discovery of three cone types (stage 1: L-long, M-middle, and S-short wavelength sensitive) and four cone-opponent mechanisms (stage 2: L+M-, M+L-, S+(L+M)-, and (L+M)+S-). We now know that these cone opponent mechanisms are generated by precise retinal circuits to give rise to four types of L/M opponent neurons and two types of S/(L+M) opponent neurons (*6-8*). These retinal ganglion cell types connect to the primary visual cortex (V1) via the lateral geniculate nucleus of the thalamus and terminate in different layers of V1. L+M-, L-M+, M+L-, and M-L+ terminate in layer 4Cβ; (L+M)+S- in layer 4A and S+(L+M)- in layer 3B blobs (*9*). The neural circuit mechanisms that give rise to color appearance (Stage 3) remain elusive, but require specific patterns of mixing between L/M and S/(L+M) cone opponent mechanisms (*1*) (Fig. 1) and therefore cannot occur before V1. These mixing patterns are based on explicit models and circuit level predictions generated by the psychophysics community to account for the appearance of the opponent colors, red and green or blue and yellow (*10, 11*), as well as "unique colors" (*1, 12-14*). Fig. 1 illustrates the cone-opponent mixing patterns that are required to account for the perception of opponent colors and unique hues (*1*). Specifically, color opponency forbids mixtures of L+ with M+, L- with M-, and S+ with S- (combinations that would create achromatic responses), while the appearance of each of the four "unique colors" (red – RG; green – GR; yellow – YB; blue – BY) requires a particular mixture of the four remaining combinations between L/M opponent and S+ or S- mechanisms, which are L+S+, M+S-, L+S-, M+S+, respectively.

Here we present data showing that these predictions are implemented by functionally-organized circuits in the superficial layers of V1. We developed intrinsic signal imaging (ISI) methods to map the locations in V1 that are responsive to the ON and OFF phases of cone-isolating stimuli. These maps reveal cone-opponent functional domains (COFDs) where neurons are preferentially activated by the ON or OFF phases of cone-isolating stimuli. Results show that L-ON (L+) and M-OFF (M-) responsive regions are always spatially overlapping, as are L-OFF (L-) and M-ON (M+) regions, to generate L+M- and M+L- domains. The L+M- and M+L- domains occur as adjacent non-overlapping pairs. S+ and S- domains are also organized as non-overlapping pairs. Importantly, the axes joining the L+M-/M+L- pairs are often organized roughly orthogonally or interdigitated in parallel to the axes joining nearby S+/S- pairs, to create interactions across all four combinations. The same relationships are observed for the underlying individual neurons assayed with 2-photon calcium imaging (2PCI) and the intersections of the interacting pairs often form hue "pinwheels" or parallel structures. These combinations correspond to the circuits predicted to generate color-opponency and unique hues RG, GR, YB and BY in third stage mechanisms (Fig. 1). Finally, ISI hue-phase maps and 2PCI of individual neurons reveal that the functional architecture and micro-architecture of neuronal color preferences within intersecting COFDs is as expected from relatively linear combinations of these cone-opponent mechanisms, indicating that circuits in these regions do in fact implement the predicted mixing.

Results

We conducted ISI and 2PCI to map the functional architecture and measure the visual responses of neurons in superficial layers of V1 using methods described previously (*15*). Here we present data collected from 7 adult male and female macaque monkeys (*M. fascicularis*) (see Table S1). All data were collected from anesthetized animals following procedures approved by the Salk Institute Institutional Animal Care and Use Committee. We present ISI data from 5 animals (A1, A2, and A5 to A7) and 2PCI data from 3 animals (A1, A3, A4). Data from 2 of the animals (A3, A4) subjected to 2PCI has been described in a previous publication (*15*), but data presented here include responses to visual stimuli and analyses not described in the previous publication.

Cone-opponent functional domains in V1

We used the 2PCI and ISI imaging methods described above to reveal cone-opponent functional domains in V1. We begin by describing the functional micro-architecture of cone inputs to individual neurons measured with 2PCI imaging. We presented flashed sine-wave gratings (Fig. 2A) while monitoring changes in fluorescence of superficial V1 neurons (150-310 μm depth, Fig. 2, B to H) expressing the genetically-encoded calcium indicator GCaMP6f (Fig. 2, C and D). These sine-wave gratings consisted of 4 sets with different colors which were L, M, or S cone-isolating or achromatic, and they were presented in separate stimulus blocks. Each set was generated using the same Hartley basis function (*16*), therefore, the orientations, spatial frequencies (SFs), and spatial phases were identical between each set (see materials and methods). Fluorescence changes were converted to inferred spike-rate time sequences that were then used to calculate spike-triggered averages (STA) of stimuli as linear estimates of receptive fields (Fig. 2, E to H). 2PCI from 9 imaging regions (16 planes, 1168 x 568 μm or 1100 x 725 μm) yielded data from 13117 neurons that were visually responsive to drifting gratings (see materials and methods). A subset of those visually responsive neurons (2420 of 13117 neurons, 18.4%) had significant STA kernels (see materials and methods) to one or more of the Hartley stimulus sets. These included 1578 neurons with significant STAs to the achromatic stimulus set, 596 to L-cone isolating, 607 to M-cone, and 600 to S-cone. That only a minority of neurons have significant STA kernels is expected from the prevalence of complex cells in superficial V1 that do not linearly integrate responses to flashed grating stimuli. The smaller numbers of neurons responsive to L and M cone-isolating versus achromatic stimuli is expected from the low cone-contrasts of the L and M cone-isolating stimuli (18%-18.5%, L and M cone-contrasts were matched, see materials and methods) imposed by the properties of the CRT monitor, versus 98%-99% achromatic stimulus contrast. The small minority of neurons with significant S-cone STA kernels cannot be attributed to the cone contrast of the S-cone stimulus, which was 89.9%-90.2%.

If a neuron had a significant STA kernel to a Hartley stimulus set, then we calculated its ON or OFF dominance (see materials and methods), and plotted the ON/OFF dominance map in red/blue, based on the locations of neurons. Maps from all imaging regions are presented in the main and supplementary figures (Fig. 2, Fig. 3, and fig. S1). Here, we call attention to representative examples from two imaging regions in Fig. 2 (I and J) and Fig. 3 (F to I). In all imaging regions, neurons with significant STA kernels occupied a small and relatively contiguous region within the imaging window. This organization is best appreciated in the context of maps showing the locations of all visually responsive neurons, relative to the locations of neurons with significant STA kernels (in Fig. 3, compare F to I with J). It is apparent from these maps that neurons with dominant responses to the ON versus OFF phases of each stimulus set are clustered together for each of the four stimulus sets. Furthermore, clusters of neurons with L-ON dominance overlap with M-OFF dominance clusters, while L-OFF clusters overlap with M-ON. The smaller numbers of neurons with significant S-cone STA kernels prevents definitive identification of the spatial relationships of S-ON and S-OFF clusters to the L and M clusters based on this relatively subjective assessment. (We present detailed neuron-by-neuron comparisons of the signs and magnitudes of cone weights to each cone-isolating stimulus below, Fig. 5H). These cone and achromatic ON/OFF dominance maps suggest that within V1 there are functional architectures where neurons with significant STA kernels are clustered together, that ON and OFF dominant neurons of each type are further clustered, and that the organized overlap between L and M cone clusters creates L+M- and M+L- cone-opponent clusters.

We inferred that this cone-opponent functional architecture might be visualized across much larger V1 regions using ISI and allow its relationship to cytochrome oxidase (CO) “blobs” and “interblobs” (*17*) to be revealed by aligning ISI maps to postmortem CO histology (*15*). To generate ISI ON/OFF phase maps corresponding to the ON/OFF phases of L, M and S cone-isolating and achromatic stimuli, we presented full-field stimuli that were temporally modulated between ON and OFF phases of each stimulus type at 0.017 Hz, 0.08Hz or 0.1 Hz (Fig. 3A, see materials and methods). Subsequent Fourier analysis of the ISI images yielded ON/OFF phase maps for each stimulus type (*18*) (see materials and methods). In all 5

animals imaged, and in response to each stimulus type, the phase maps showed clear patches of ON and OFF signal surrounded by regions with no phasic response, extending across the full extent of V1 (Figs. 3, 4, 6, and figs. S1 and S3B). (Phase maps in the adjacent visual cortical area V2 are not further explored here.) Furthermore, within each patch, there were invariably adjacent pairs of alternating ON and OFF domains. Because of the unknown latency of hemodynamic signal, correct signs cannot be assigned to the phase maps without additional measurements from another modality with greater temporal sensitivity. We identified the correct phases using electrophysiological recordings (see materials and methods and fig. S7) within imaged domains for 2 of 5 animals (A2, A5) and using 2PCI for 2 of the remaining animals (A1, A6). For the last animal (A7), similar phase maps were generated (fig. S3B), but we did not identify the phase signs. We assume that the latency is consistent between every sub-region within V1 for each animal. Alignment of ISI phase maps to the ON/OFF dominance map measured by 2PCI demonstrates a clear correspondence between the two imaging modalities (Fig. 3, F to I, and fig. S1). We refer to the V1 regions with strong ON and OFF phasic responses to temporally modulated cone-isolating stimuli as cone-opponent functional domains (COFDs).

COFD interactions follow color appearance mixing rules

Based in their spatial overlaps, the COFDs in V1 appear to follow the cone-opponent mixing rules predicted by studies of color appearance (Fig.1). In particular, L-ON functional domains overlap with M-OFF and L-OFF overlap with M-ON, but there is minimal overlap between L-ON and L-OFF or between M-ON and M-OFF (Fig. 4, A, B, D, E, and G). This overlap generates L+M- and M+L- domains that appear to intersect with both S+ and S- domains (Fig. 4H). Two different types of intersections appear to be common within these maps. In many cases, an isolated set of COFDs includes one L+M-/M+L- pair and one S+/S- pair, in which the axes connecting the L/M COFDs are perpendicular to the axes connecting the S COFDs (e.g. *dark arrows* in Fig. 4H, schematic in Fig. 4I). Other interactions occur through a parallel arrangement, with S+ and S- domains interdigitated between the L+M- and M+L- domains (e.g. *bright arrows* in Fig. 4H, schematic in Fig. 4I). These spatial relationships potentially allow the S+ and S- domains to mix with the L+M- and M+L- domains in the combinations predicted by color appearance models (Figs. 1 and 4I), suggesting that the COFDs are the substrate for implementation of the cone-opponent mixing rules that generate color opponent mechanisms.

We next quantified the relationships between the L, M, and S-COFDs to more rigorously test this possibility. The COFD map of each cone type was thresholded to generate a mask to select ON- and OFF-phase regions, then masks from all three cone type maps were merged to create a final COFD mask including L, M and S-COFD regions. Then using normalized pixel values from L, M, and S-COFD maps (range: [-1 to 1]), each pixel within the COFD mask was assigned three values corresponding to the modulation (including magnitude and sign) by each of the three cone-isolating stimuli at that pixel (see materials and methods). Pixel-by-pixel comparisons were then made across each of the three possible comparisons of cone-types (M to L, S to L, and S to M). Typical results are illustrated in Fig. 4, M to O. Similar results were observed for all 4 animals with known ON/OFF phases (Fig. 4 and figs S3A). It can be seen that for the L-cone versus M-cone comparisons, the great majority of pixels (84.2%) fall into the LM opponent quadrants (L+M- and M+L-) and not in the achromatic quadrants (L+M+ and L-M-). In contrast, comparisons between S-cone and either L- or M-cone maps generate pixels relatively evenly distributed across all 4 quadrants, as predicted. While it can be appreciated that achromatic ON and OFF domains have a similar appearance and overall organization as COFDs (Fig. 3, E and I, and fig. S1), we do not systematically explore their spatial relationships here. (But see below for relationships of COFDs and achromatic domains to CO histology.)

COFD interactions generate hue tuning maps in DKL color space

The above observations show that the overlap of the COFDs follows the rules required to generate appropriate mixing for color opponency, but do not reveal whether mixing occurs at the level of individual neurons or how neurons within the overlapping regions respond to a larger range of hues. For example, are the ISI phase responses to colors that concurrently modulate multiple cone types predictable from the COFD maps, as expected from mixing of cone-opponent inputs? Do the individual neurons within the COFDs prefer colors that would be predicted from mixing of the cone-opponent mechanisms within the COFDs?

To address these questions, we selected as visual stimuli a set of 12 hues spaced evenly in the isoluminant plane of DKL color space (*19*) (see materials and methods), which were presented as drifting gratings for 2PCI or temporally modulated gratings for ISI, and imaged the responses of neurons within the COFDs. We generated both ISI hue-phase maps (Fig. 4, J to L, and Fig. 5, B to E), and 2PCI hue maps (Fig. 3J and fig. S2) to reveal the overall functional architecture and the microarchitecture of hue preferences of individual neurons. We chose the DKL isoluminant plane because there is a close correspondence between DKL colors and the cone-opponent mechanisms, allowing straightforward predictions of hue preferences expected from linear integration of cone-opponent inputs. Within the DKL isoluminant plane, hue angles of 0 and 180 deg. correspond to the L+M- and M+L- directions and appear pinkish and greenish, respectively, while 90 and 270 deg. correspond to S+ and S- and appear violet and lime (Fig. 5A, and fig. S6B). Intermediate hues are predicted from mixing of the cone-opponent mechanisms that modulate along these cardinal axes. The L, M, and S cone increments were matched for the DKL stimuli presented to animal A1 (both ISI and 2PCI experiments), while for animal A2 (ISI experiments only) all cone increments were set to the maximum cone contrasts achievable with the monitor, substantially increasing the S-cone contrasts relative to L and M cone contrasts (see materials and methods and fig. S6B). These differences are noted where relevant, below.

Figure 3J illustrates, for one imaging region (out of 5 sampled), the 2PCI-based functional microarchitecture for hue preferences in the DKL isoluminant plane (matched cone increments) and the overlaps with COFD maps are shown in Fig. 3, K to L. (Maps from all 5 imaging regions, 10 planes, are shown in fig. S2). All visually responsive neurons are indicated, with significantly hue-selective (see materials and methods) neurons identified by their preferred hue and non-selective neurons in grey. It is readily apparent that neurons with similar hue preferences are grouped together and that hue preferences shift gradually across the cortical surface (Fig. 3J, and fig. S2). When overlaid on the M-cone ISI phase map, it is apparent that neurons in the M+ (L-) domains prefer greenish hues while those in the M- (L+) domains prefer pinkish hues (Fig. 3K). The predominant red and greenish preferring neurons are both found in both S+ and S- domains (Fig. 3L).

To quantitatively evaluate the relationships between the preferred DKL hues of individual neurons and their locations within ISI COFD maps, we first selected neurons located within COFDs and that were significantly tuned to DKL hues (n = 2589 neurons from 5 imaging regions). We then generated a mask for each neuron to identify its corresponding ISI pixels and the normalized pixel values from L, M, and S-COFD maps (see above) for each neuron were averaged to yield the magnitudes and signs modulated by L, M and S cone-isolating stimuli. Similar to Fig. 4, M to O, three possible comparisons of cone-types (M to L, S to L and S to M) were plotted neuron-by-neuron (Fig. 4, P to R), and each neuron was colored according to its preferred DKL hue measured by 2PCI. For the L cone versus M cone plot (Fig. 4P) pixels from the great majority of neurons (87.1%) are in the L/M opponent quadrants; neurons with pixels in the L+M- quadrant are significantly more likely to prefer DKL hues near 0 deg. (0 ± 60 deg., 1167 of 1650 neurons, 70.7%) than near 180 deg. (180 ± 60 deg., 462 of 1650 neurons, 28.0%; $P < 0.0001$, Fisher's exact test); and neurons with pixels in the M+L- quadrant are significantly more likely to prefer hues around 180 deg. (180 ± 60 deg., 344 of 605 neurons, 56.9%) than around 0 deg. (0 ± 60 deg., 250 of 605 neurons, 41.3%; $P = 0.0018$, Fisher's exact test). For the S-cone versus L and M cone comparisons (Fig 4, Q and R) neurons are more evenly distributed amongst the 4 quadrants, as expected from the overlap of both S+ and S- domains with all combinations of L and M cone domains.

Perceived color is influenced not only by the relative activation of different cone types, but also by luminance, or achromatic contrast. For example, the DKL color space (like other color spaces) includes modulation not only in the isoluminant plane, as we have explored here, but also along the achromatic axis(*19*). While we have observed achromatic ON and OFF phase maps similar to the COFDs (Fig. 2J and Fig. 3, E and I), we have not explored the responses of individual neurons to the much larger 3D hue stimulus space. Future studies should explore whether the achromatic ON and OFF domains interact with the COFDs to generate predictable tuning across the full 3D color space.

Consistent with these 2PCI results indicating mixing of cone-opponent mechanisms to generate intermediate hue-selectivities of individual neurons within COFDs (above), we also observed gradual shifts in ISI hue-phase maps (Fig. 5, B to F, and fig. S4A) generated with stimuli modulated at non-cardinal directions in the DKL isoluminant plane (Fig. 5A). These maps were generated using DKL stimuli with cone increments maximized (non-matched, see above) to better reveal the locations with responsiveness to S-cones. The gradual shifts in ISI hue-phase maps are quantified in Fig. 5, F and G. Similar to comparisons of normalized ISI phase pixel values and signs across maps from the cone isolating stimuli (Fig. 4, M to O), each row of Fig. 5F illustrates comparisons between pixel values from each of the 12 hue-phase maps with either the L (top row), M (middle row) or S cone (bottom row) phase maps. It can be seen that as DKL hue directions shift, the phase relationships to the COFD phases shift gradually (Fig. 5, F and G, and fig. S4, A and B). When hue directions are near the L/M axis (0 and 180 deg.) pixels are in opposing quadrants in relationship to the L and M phase maps (Fig. 5F and fig. S4B) and accordingly the angles joining the two clusters of pixels in each plot are near 45 and 135 deg. (Fig. 5G and fig. S4C). When these hue phase maps (0 and 180 deg. hues) are related to the S-cone phase maps, the pixels occupy all 4 quadrants (Fig. 5F and fig. S4B) and joining angles are near 90 deg. (Fig. 5G and fig. S4C). As hue directions gradually increase in S cone modulation, comparisons to the L and M phase maps show pixels gradually occupying all 4 quadrants (Fig. 5F and fig. S4B) and joining angles gradually shifting (Fig. 5G and fig. S4C), until at maximal S cone modulation (90 and 270 deg.), all 4 quadrants are occupied and joining angles are near 90 deg. In contrast, comparisons of hue phase maps to the S-cone maps show pixels more evenly distributed across all 4 quadrants, with the exception of comparisons to the S+ and S- hues (90 and 270 deg.) where opposing quadrants are occupied (Fig. 5F and fig. S4B) and joining angles are near 45 and 135 deg. (Fig. 5G and fig. S4C). These observations indicate that, not only does the overlap between COFDs follow the rules predicted to generate color appearance mechanisms (Fig. 1, and Fig. 4, M to O), but that the interactions between L, M, and S-COFDs generate preferential responses to intermediate hues within the DKL color space, as predicted from those interactions (Fig. 4, P to R, Fig 5, F and G, and fig. S4, B and C).

Surprisingly, we also noted that plots of these hue maps across the 360 degrees of DKL color space often resulted in pinwheel-like structures within hue angle maps (Fig. 4, J to L, arrows highlight selected pinwheel centers), reminiscent of the well-known orientation pinwheels that are also found in V1 (see also orientation and hue polar maps in fig. S2). Similar to methods typically used to calculate orientation polar maps, the hue-phase-regions from 12 hue-phase maps were selected, vectorized and summed pixel-by-pixel to generate the hue angle or polar map (see materials and methods). In some striking cases the pinwheel centers correspond precisely to regions of convergence of L+M-/M+L- COFD pairs with S+/S- pairs whose axes are arranged orthogonally (Fig. 4, H, J and K, dark arrows; note that H, J and K are the same region; J and K are the same map, but K is overlaid with the same contours from H), but other pinwheel centers are found where COFD pair axes interact in a more parallel arrangement, and some are even found outside the COFDs. DKL hue pinwheels were most apparent when generated using stimuli with cone increments maximized (Fig. 4, J and K), but were also observed when cone increments were matched (Fig. 4L).

Cone inputs and hue tuning

For 2PCI-assayed neurons with significant STA kernels to the L, M, or S cone-isolating Hartley stimulus set, their preferred directions in color space were also highly consistent with the magnitude and sign of cone inputs estimated from the STA kernels. This was the case both for hues presented in the DKL isoluminant

plane (Fig. 5H) and in CIE color space (Fig. 5L, see materials and methods, (*15*)). This relationship is most apparent from the responses to DKL hues, due to the clear correspondence between cone-opponency and DKL hue directions. Normalized cone weight plots (see materials and methods) for both DKL and CIE hues (Fig. 5, H and L) show that the great majority of neurons are in the L+M- and M+L- cone-opponent quadrants, as expected from the mixing described above. Neurons in the achromatic quadrants have only weak STAs to one or another of the L or M cone-isolating stimuli, as expected from the noise inherent to calculation of input magnitude from STA kernels and the methods we used to assign values (see materials and methods). (Neurons with a significant STA to only one stimulus set were nevertheless assigned values for the non-significant stimuli rather than pinning values to zero.) As expected, for the neurons tested with DKL hues, the great majority of hue-selective neurons in the L+M- quadrant preferred DKL directions around 0 deg. (315 of 390 = 80.8% of neurons at 0 ± 60 deg.), while those in the M+L- quadrant preferred DKL directions around 180 deg. (119 of 213 = 55.9% of neurons at 180 ± 60 deg.). For neurons tested with CIE hues, hue-selective neurons in the M+L- quadrant nearly all preferred blue while neurons in the L+M- quadrant mostly preferred red with some preferring blue (Fig. 5L). This arrangement is expected from the stronger L cone contrast for red and stronger M cone contrast for blue (fig. S6C), combined with the fact that the OFF phase of the blue stimulus can sometimes generate a stronger L response than M. It is important to note that hue selective neurons generate both ON and OFF responses to drifting hue gratings and due to the slow dynamics of calcium signals observed with 2PCI, it is not possible to definitively identify whether responses are being generated to the ON versus the OFF phases of the drifting gratings. While ON responses are generally stronger than OFF responses, this may not always be the case. Therefore, the hue preferences observed from 2PCI imaging of responses to drifting gratings are not expected to always match the predictions from responses to flashed, cone-isolating stimuli.

There is also a clear separation of a set of neurons near the middle of the diamond plots with relatively strong S-cone STA kernels (Fig. 5, H and L). Note that the S-cone isolating stimulus used to generate these STA kernels is much higher contrast (89.9%-90.2%) than the L and M-cone stimuli (18%-18.5%), contributing strongly to the separation of this group. This is apparent from the overall distribution of hue preferences to DKL stimuli (Fig. 5I). Here it can be seen that when stimuli are matched for cone increment magnitude (see materials and methods), responses are dominated by colors modulated at or near the L-M opponent axis (0 and 180 deg.). Extremely few (138 of 6658 neurons, 2.07%) preferred stimuli modulated in the S+ or S- directions. Nevertheless, S-cone inputs could be seen to have a significant, although relatively weak influence on preferred DKL hue. Amongst neurons with significant S-cone STA kernels, their preferred directions in the DKL isoluminant plane were consistent with expected shifts resulting from linear integration with L/M opponent mechanisms. Neurons with significant S-cone ON STA kernels were more frequently tuned to the DKL hue at 90 deg. than neurons lacking significant S-cone STA kernels (7 of 203 neurons, 3.45% versus 52 of 6167 neurons, 0.84%; $P = 0.0058$, Fisher's exact test), or than neurons with significant S-cone OFF STA kernels (0 of 288 neurons, $P = 0.0045$, Fisher's exact test). Similarly, neurons with significant S-cone OFF STA kernels were more likely to prefer the DKL hue at 270 deg. than neurons without significant S-cone kernels (9 of 288 neuron, 3.13% versus 70 of 6167 neurons, 1.14%; $P = 0.0184$, Fisher's exact test), or than neurons with significant S-cone ON STA kernels (0 of 203 neurons, $P = 0.0175$, Fisher's exact test).

Preferred hues within COFDs and their intersections

The relatively weaker influence of the S cone relative to the L/M opponent mechanisms during interactions between the COFDs can be seen not only in the hue tuning of the individual neurons (see above), but also in the tuning of ISI pixels within the different COFDs to the DKL stimuli. To further quantify the relationships between COFDs and DKL hue responses, the COFD masks were used to identify pixels in each COFD ON or OFF region (Fig. 5P and fig. S4D), as well as intersections between regions (Fig. 5Q and fig. S4E), and then the ISI hue responses of those pixels were used to generate hue tuning curves. For example, it can be seen in Fig. 5P that, as expected, the pixels in the L+ and M- COFDs were most strongly

modulated by hues at or near the 0 deg. hue direction and most weakly modulated by the 180 deg. hue direction. In contrast, the M+ and L- pixels were most strongly modulated at 180 deg. and least strongly at 0 deg. Importantly these tuning curves are relatively symmetric around the 90 to 270 deg. axis, as expected from near equal influences of S-ON and S-OFF signals, resulting from the symmetric mixing of S-ON and S-OFF COFDs with the L+M- and M+L- domains. Also as expected, the S+ COFDs responded more strongly to 90 deg. than to 270 deg. and S- more strongly to 270 deg. than to the 90 deg. hue. But owing to the relatively weak S cone influence, responses to the intermediate as well as 0 and 180 deg. hues were at least as strong as those to 90 or 270 deg.

To more directly assess the predictions from mixing of COFDs to generate color opponent signals, we also generated DKL hue tuning curves for the pixels at the intersections corresponding to the regions where neurons would be expected to be shifted toward each of the red (L+ ∩ S+), yellow (L+ ∩ S-), blue (M+ ∩ S+), and green (M+ ∩ S-) color appearance mechanisms (Fig. 5Q and fig. S4E). As expected from their L+ contributions, the "red" (e,g. L+ ∩ S+) and "yellow" pixels were strongly biased to preferences toward 0 deg. and away from 180 deg. hues. Similarly, the pixels corresponding to "colors" with M+ contributions ("blue" and "green") had DKL hue preferences that were strongly biased toward 180 deg. and away from 0 deg. Importantly, it can be seen that the differential mixing of S+ and S- for each of the combinations generates differential shifts toward or away from the S+ (90 deg.) and S- (270 deg.) DKL hues. Specifically, the "red" pixels have hue preferences that are shifted toward 90 deg. (away from 270 deg.) relative to the "yellow" pixels, and the "blue" are similarly shifted relative to the "green" pixels. Again, despite the clear differences between the intersections with S+ versus S- COFD contributions, the shifts along the 90-270 axis are much smaller than the shifts along the 0-180 deg axis, once again reflecting the weak overall contributions of the S cone inputs. This imbalance can also be visualized by comparing to an idealized schematic that assumes balanced interactions across the COFD intersections (Fig. 5R). Fig. 5R also serves to illustrate the hypothesized production of hue pinwheels that we have described at some locations where the physical positioning of COFDs generates interactions across orthogonal S+/S- and L+M-/M+L- axes (Fig 4, H to L). In such cases, the conceptualized schematic and the actual physical mapping on the brain have similar configurations.

COFDs and CO histology

Previous studies have suggested that cytochrome oxidase blobs in layer 2/3 are specialized for processing of color information ((*20*), but see(*21*)), receive direct S+ input from the LGN (*9, 22*), and could have neurons with a different distribution of preferred colors than interblobs (*15*). We were therefore interested in whether there might be a relationship between COFDs and CO staining, either for all COFDs together (data from all 5 animals) or for ON or OFF domains of particular cones (animal A7 excluded). Alignment of COFD maps to postmortem CO histology ((*15*) and see materials and methods) shows that they have similar periodicity and are often overlapping, but there are also clearly regions that do not overlap (Fig. 3M and Fig. 6, E and F). To quantify these relationships, the distributions of CO intensities were compared between pixels located within versus outside all COFDs. Complete results from all comparisons for all imaging regions are shown in fig. S5A. In general, regardless of the cone type (L, M, S) or phase (ON or OFF), pixels in the COFDs have higher CO intensities and pixels in non-COFD regions have lower CO intensities than expected from the overall distribution of CO intensities across V1. The biases of these COFD regions toward high CO intensities were all significant for every animal (4 animals for comparisons between phase-identified COFDs with non-COFDs, 5 animals for comparisons between phase-unassigned COFDs with non-COFDs). These statistical comparisons within animals are based on treatment of each COFD region as an independent sample (see materials and methods, Wilcoxon signed rank test), and P values less than 0.05 are considered significant. Across animals, the bias toward high CO intensities is statistically significant (n = 5 animals, P = 0.03125, right-tailed Sign test) only for the comparisons based on phase-unassigned COFDs (5 animals), as maximal statistical significance for 4 animals is P = 0.0625.

The achromatic ON and OFF domains were also significantly biased toward blob regions for all 3 animals in which achromatic phase maps were generated.

Because a previous study has shown that S+(L+M)- LGN afferents preferentially terminate in the CO blobs (*9*), we were particularly interested in whether S+ domains might be more strongly biased toward high CO intensity regions than other COFDs. Comparisons between cone types and phases within animals revealed consistent significant differences only for the S+ domains, which were significantly biased toward higher CO intensities than S- for all four animals (see materials and methods, Wilcoxon rank sum test, *P* values less than 0.05 are considered significant, and the same test method and criteria were applied on the following comparisons). S+ was also significantly higher than both L+ and M- in 3 of 4 animals. Other comparisons were significant for only 1 or 2 out of the 4 animals. It is noteworthy that the most dense S+ LGN terminals and CO staining are found deep within layer 2/3 (layer 3B) (*9, 22*), so there might be a closer correspondence between S+ responses and CO deeper in cortex.

Previous studies have used ISI and colored visual stimuli to reveal patchy activation patterns ("color domains") within V1 (*23, 24*). We have generated maps using the same methods applied in those studies (regions preferentially responsive to red/green or blue/yellow isoluminant stimuli) and directly compared those maps to COFDs imaged in the same animals. We find that the color domains and COFDs are closely related (fig. S5B). This is expected, because both red/green and blue-yellow isoluminant modulation should differentially activate selected regions within the COFDs. The partial but not exclusive correspondence between COFDs and CO histology is also consistent with previous observations of the relationships between color domains and CO staining (*24*).

Discussion

In summary, we have demonstrated that: 1) L, M and S COFDs are a prominent feature of the functional organization of primate V1 that can be readily revealed with ISI imaging; 2) 2PCI-assayed responses of neurons within the COFDs have ON and OFF responses to cone-isolating stimuli that correspond to ISI phase maps; 3) both qualitative and quantitative assessment of the spatial intersections of COFDs shows that they follow the mixing rules predicted from models of color appearance mechanisms; 4) DKL-hue phase maps show that the hue preferences at intersections between COFDs correspond to hues predicted from functional mixing and generate hue pinwheels; 5) 2PCI of DKL hue preferences at the intersections of COFDs shows that functional mixing occurs at the level of individual neurons; and 6) COFDs are biased toward regions of high CO intensity. We conclude that the neural substrates that underlie the transition from cone-opponent (stage 2) mechanisms to color opponent (stage 3) mechanisms are highly organized and implemented by specific connections between neurons in the geniculate input layers (4C, 4A, 3B) and the neurons that we have assayed in more superficial V1.

The most prominent feature of stage 3 of the 3 stage model is the specific combinations of mixing between cone-opponent mechanisms that are predicted to give rise to each of the four color-opponent mechanisms (Fig. 1). This mixing is expected to generate a greater range of hue preferences than is present in the cone-opponent geniculate input population, largely owing to the interactions between the L/M and S/(L+M) mechanisms that do not occur at earlier stages. The "unique colors" (red, green, blue and yellow) are not necessarily expected to be preferred by larger numbers of neurons than other hues, but instead reflect perceptual transitions within the color opponent mechanisms, where, for example, "red" appears neither "bluish" or "yellowish" (*1*). (Due to the opponent nature of color appearance, red cannot appear "greenish" (*11*).) Consistent with these expectations, our observations and analyses indicate that mixing of the L/M opponent mechanisms with S/(L+M) mechanisms within COFDs gives rise to shifts in preferred hues that are in the directions expected to generate color opponent mechanisms. But the contribution of the S/(L+M) mechanism is likely much less than expected to fully account for color appearance. Careful calculations based on psychophysical measures assign just a 2.55-fold stronger influence to the L/M mechanism (*1*), while the responses we have measured from neurons in upper layer 2/3 of V1 appear to reflect a much

stronger relative influence of the L/M mechanism. It is likely that these relative contributions are re-weighted in higher visual areas, as suggested by a recent 2PCI study comparing responses to CIE hues in cortical areas V1, V2, and V4 (*25*). Importantly, our observations using DKL hues show that the biases of V1 neurons toward end-spectral CIE colors observed previously (*15, 25*) do not result solely from the stronger L and M cone activation generated by the red and blue CIE hues (*15, 26*); S-cone contributions are weak even in response to DKL stimuli with matched L, M, and S-cone increment magnitudes. Neurons deeper in layers 2/3 and 4A (inaccessible to 2PCI) that receive direct S/(L+M) signals (*9*) and can project directly to V2 might also have more dominant S-cone influences that could contribute to stronger S cone influences in higher visual areas.

Electrode penetrations extending across cortical layers have also found locations containing neurons with Blue-Yellow versus Red-Green opponency, leading to the suggestion that there are separate blobs for each type of opponency (*27*). The COFDs that we observe, as well as their relationships to CO staining, argue against this interpretation and provide an explanation for why different electrode penetrations might sometimes be biased to sample neurons with different color opponency. There may in fact be color columns that extend across cortical layers, but they likely correspond to the more closely spaced COFDs with different cone inputs rather than to separate blobs. Future experiments using ISI imaging of COFDs to guide subsequent electrode penetrations (e.g. fig. S7) should more clearly reveal the extent to which color selectivities and/or cone input signs and sensitivity extend across or vary between layers.

We have observed a functional organization (COFDs) in the most superficial layers of V1 that involves systematic mixing of L/M opponent with S+ and S- signals. The fact that L/M opponent LGN inputs terminate in a separate layer (layer 4Cβ) from S+ (layer 3B) and S- inputs (layer 4A) indicates that mixing of these cone-opponent systems can only occur through neural substrates that span across these layers and also suggests that there are likely to be some laminar differences in cone responses and color tuning. The most prominent substrate for potential mixing is the axons of layer 4Cβ spiny stellate neurons that extend to and densely arborize in layers 4A and 3B, likely mixing L/M opponent with S cone signals (*28, 29*). Yet another synaptic step is required to transmit information in layer 4A/3B to the neurons that we imaged in layer 2/3A (*30*). An additional possibility that should not be overlooked is a specialized population of layer 6 pyramidal neurons (Type IβA) that have both dendritic and axonal processes that arborize selectively in both layers 4Cβ and 4A/3B (*31-33*). These neurons could directly integrate L/M opponent with S+ or S- LGN inputs and provide their mixed signals to neurons in layers 4Cβ and 4A/3B. Such a mechanism could account for Blue-Yellow opponent neurons that have been reported in layer 4C (*27*). While our observations clearly point to these circuits as the neural substrates that mediate mixing of cone-opponent mechanisms to generate the rudiments of color opponency, further experiments will be required to more precisely identify the micro-circuitry involved.

References and Notes:

1. A. Stockman, D. H. Brainard, in *OSA handbook of optics,* M. Bass, Ed. (McGraw-Hill, New York, 2010), chap. 11, pp. 11.11-11.104.
2. D. B. Judd, Fundamental studies of color vision from 1860 to 1960. *Proc Natl Acad Sci U S A* **55**, 1313-1330 (1966).
3. D. B. Judd, Response functions for types of vision according to the Muller theory. *J Res Natl Bur Stand (1934)* **42**, 1-16 (1949).
4. G. E. Muller, Über die Farbenempfindungen. *Zeitschrift für Psychologie und Physiologie der Sinnesorgane, Ergänzungsband* **17**, 1-430 (1930).
5. R. L. De Valois, K. K. De Valois, A multi-stage color model. *Vision Res* **33**, 1053-1065 (1993).
6. D. M. Dacey, Parallel pathways for spectral coding in primate retina. *Annu Rev Neurosci* **23**, 743-775 (2000).
7. L. E. Wool, O. S. Packer, Q. Zaidi, D. M. Dacey, Connectomic Identification and Three-Dimensional Color Tuning of S-OFF Midget Ganglion Cells in the Primate Retina. *J Neurosci* **39**, 7893-7909 (2019).
8. G. D. Field *et al.*, Functional connectivity in the retina at the resolution of photoreceptors. *Nature* **467**, 673-677 (2010).
9. S. Chatterjee, E. M. Callaway, Parallel colour-opponent pathways to primary visual cortex. *Nature* **426**, 668-671 (2003).
10. L. M. Hurvich, D. Jameson, An opponent-process theory of color vision. *Psychol Rev* **64, Part 1**, 384-404 (1957).
11. E. Hering, *GRUNDZÜGE DER LEHRE VOM LICHTSINN*. (Springer, Berlin, 1920).
12. R. L. De Valois, K. K. De Valois, E. Switkes, L. Mahon, Hue scaling of isoluminant and cone-specific lights. *Vision Res* **37**, 885-897 (1997).
13. J. D. Mollon, G. Jordan, in *John Dalton's Colour Vision Legacy,* I. M. D. C. C. Dickinson, Ed. (Taylor and Francis, London, 1997), pp. 381-392.
14. J. Krauskopf, in *Color Vision: From Genes to Perception,* K. R. Gegenfurtner, L. T. Sharpe, Eds. (Cambridge University Press, New York, 1999), pp. 303-317.
15. A. K. Garg, P. Li, M. S. Rashid, E. M. Callaway, Color and orientation are jointly coded and spatially organized in primate primary visual cortex. *Science* **364**, 1275-1279 (2019).
16. D. L. Ringach, G. Sapiro, R. Shapley, A subspace reverse-correlation technique for the study of visual neurons. *Vision Res* **37**, 2455-2464 (1997).
17. J. C. Horton, D. H. Hubel, Regular patchy distribution of cytochrome oxidase staining in primary visual cortex of macaque monkey. *Nature* **292**, 762-764 (1981).
18. V. A. Kalatsky, M. P. Stryker, New paradigm for optical imaging: temporally encoded maps of intrinsic signal. *Neuron* **38**, 529-545 (2003).
19. A. M. Derrington, J. Krauskopf, P. Lennie, Chromatic mechanisms in lateral geniculate nucleus of macaque. *J Physiol* **357**, 241-265 (1984).
20. M. S. Livingstone, D. H. Hubel, Anatomy and physiology of a color system in the primate visual cortex. *J Neurosci* **4**, 309-356 (1984).
21. K. R. Gegenfurtner, D. C. Kiper, Color vision. *Annu Rev Neurosci* **26**, 181-206 (2003).
22. M. S. Livingstone, D. H. Hubel, Thalamic inputs to cytochrome oxidase-rich regions in monkey visual cortex. *Proc Natl Acad Sci U S A* **79**, 6098-6101 (1982).
23. H. D. Lu, A. W. Roe, Functional organization of color domains in V1 and V2 of macaque monkey revealed by optical imaging. *Cereb Cortex* **18**, 516-533 (2008).

24. C. E. Landisman, D. Y. Ts'o, Color processing in macaque striate cortex: relationships to ocular dominance, cytochrome oxidase, and orientation. *J Neurophysiol* **87**, 3126-3137 (2002).
25. Y. Liu *et al.*, Hierarchical Representation for Chromatic Processing across Macaque V1, V2, and V4. *Neuron*.
26. J. D. Mollon, A neural basis for unique hues? *Curr Biol* **19**, R441-442; author reply R442-443 (2009).
27. D. Y. Ts'o, C. D. Gilbert, The organization of chromatic and spatial interactions in the primate striate cortex. *J Neurosci* **8**, 1712-1727 (1988).
28. E. M. Callaway, A. K. Wiser, Contributions of individual layer 2-5 spiny neurons to local circuits in macaque primary visual cortex. *Vis Neurosci* **13**, 907-922 (1996).
29. N. H. Yabuta, E. M. Callaway, Functional streams and local connections of layer 4C neurons in primary visual cortex of the macaque monkey. *J Neurosci* **18**, 9489-9499 (1998).
30. E. A. Lachica, P. D. Beck, V. A. Casagrande, Parallel pathways in macaque monkey striate cortex: anatomically defined columns in layer III. *Proc Natl Acad Sci U S A* **89**, 3566-3570 (1992).
31. A. K. Wiser, E. M. Callaway, Ocular dominance columns and local projections of layer 6 pyramidal neurons in macaque primary visual cortex. *Vis Neurosci* **14**, 241-251 (1997).
32. A. K. Wiser, E. M. Callaway, Contributions of individual layer 6 pyramidal neurons to local circuitry in macaque primary visual cortex. *J Neurosci* **16**, 2724-2739 (1996).
33. F. Briggs, E. M. Callaway, Layer-specific input to distinct cell types in layer 6 of monkey primary visual cortex. *J Neurosci* **21**, 3600-3608 (2001).
34. O. Sadakane *et al.*, Long-Term Two-Photon Calcium Imaging of Neuronal Populations with Subcellular Resolution in Adult Non-human Primates. *Cell Rep* **13**, 1989-1999 (2015).
35. J. J. Jun *et al.*, Fully integrated silicon probes for high-density recording of neural activity. *Nature* **551**, 232-236 (2017).
36. B. R. Conway, Spatial structure of cone inputs to color cells in alert macaque primary visual cortex (V-1). *J Neurosci* **21**, 2768-2783 (2001).
37. A. Stockman, L. T. Sharpe, The spectral sensitivities of the middle- and long-wavelength-sensitive cones derived from measurements in observers of known genotype. *Vision Res* **40**, 1711-1737 (2000).
38. D. H. Brainard, in *Human Color Vision 2nd Edition,* P. K. Kaiser, R. M. Boynton, Eds. (Optical Society of America, Washington, DC, 1996), pp. 563-579.
39. P. Li *et al.*, A motion direction preference map in monkey V4. *Neuron* **78**, 376-388 (2013).
40. R. Gatto, S. R. Jammalamadaka, The generalized von Mises distribution. *Statistical Methodology* **4**, 341-353 (2007).
41. N. V. Swindale, Orientation tuning curves: empirical description and estimation of parameters. *Biol Cybern* **78**, 45-56 (1998).
42. D. L. Ringach *et al.*, Spatial clustering of tuning in mouse primary visual cortex. *Nat Commun* **7**, 12270 (2016).
43. D. L. Ringach, R. M. Shapley, M. J. Hawken, Orientation selectivity in macaque V1: diversity and laminar dependence. *J Neurosci* **22**, 5639-5651 (2002).
44. M. Mazurek, M. Kager, S. D. Van Hooser, Robust quantification of orientation selectivity and direction selectivity. *Frontiers in neural circuits* **8**, 92 (2014).
45. G. Purushothaman, I. Khaytin, V. A. Casagrande, Quantification of Optical Images of Cortical Responses for Inferring Functional Maps. *J. Neurophysiol.* **101**, 2708-2724 (2009).
46. M. Park, J. W. Pillow, Receptive field inference with localized priors. *PLoS Comput Biol* **7**, e1002219 (2011).
47. S. L. Smith, M. Hausser, Parallel processing of visual space by neighboring neurons in mouse visual cortex. *Nat Neurosci* **13**, 1144-1149 (2010).
48. J. Niessing *et al.*, Hemodynamic signals correlate tightly with synchronized gamma oscillations. *Science* **309**, 948-951 (2005).

Acknowledgments: We thank Professor Tetsuo Yamamori's laboratory for kindly providing pAAV-TRE3-GCaMP6f and pAAV-thy1s-tTa to make AAVs used in the study. We thank the Callaway lab for support, particularly Drs. B. J. Hansen, E. J. Kim and E. Richler. We thank Drs. D. L. Ringach, A. Cheng, R. Liu, and K. J. Nielsen for their assistance and suggestions with our two-photon microscope. We thank Dr. T. P. Franken for his contribution to the ISI acquisition software. We thank Dr. I. Nauhaus for his contribution to the visual stimulus code. **Funding:** This work was supported by NIH grants EY022577 (E.M.C), NS105129 (E.M.C.), MH063912 (E.M.C.), EY028084 (A.K.G), the Gatsby Charitable Trust (E.M.C.), and the Pioneer Fund (P.L.). **Author Contributions:** P.L., A.K.G. and E.M.C. designed the experiments. P.L. designed and built the ISI setup. P.L. designed the imaging chamber. A.K.G. built the electrophysiological recoding setup. P.L. and E.M.C. performed recovery surgeries and virus injections with M.S.R. and A.K.G.'s assistance. P.L. contributed to the visual stimulus code. P.L. performed non-recovery surgeries and set up the ISI, 2PCI and electrophysiological recoding with M.S.R. and A.K.G.'s assistance. P.L., A.K.G., M.S.R. and L.A.Z. acquired the ISI, 2PCI and electrophysiological data. P.L. and M.S.R. performed the CO histology and scanned the slides. P.L. and A.K.G. contributed to the ISI data analysis code. L.A.Z., P.L. and A.K.G. contributed to the 2PCI data analysis code. P.L. analyzed the ISI, 2PCI and histology data and made the figures. L.A.Z. contributed to the electrophysiology data analysis code, analyzed the data and made the figure. E.M.C. and P.L. wrote the manuscript with contributions from all other authors. **Competing interests:** Authors declare no competing interests. **Data and materials availability:** All data and code necessary to support the paper's conclusions are present in the main text, supplementary materials, or available from the corresponding author upon reasonable request.

Supplementary Materials:

Materials and Methods

Figures S1-S7

Tables S1-S2

References (*34-48*)

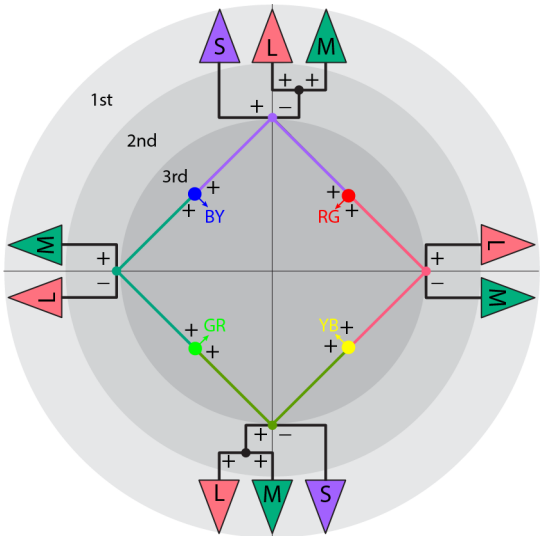

Fig. 1. Three-stage zone model of color vision (adapted from Stockman and Brainard (*1*)). At the first stage (outer ring), light is transduced by three types of cone photoreceptors, L (long), M (middle), and S (short) -wavelength sensitive. In the second stage, cone signals are integrated through four cone-opponent mechanisms (L+M-, M+L-, S+(L+M)- and (L+M)+S-) instantiated by retinal circuits connecting specific cone types to retinal ganglion cell types. At the hypothesized third stage, cone-opponent signals are predicted to combine in four specific combinations to generate color-opponent mechanisms, as well as neurons whose activities underlie the perception of four "unique colors" (red – RG; green – GR; yellow – YB; blue – BY).

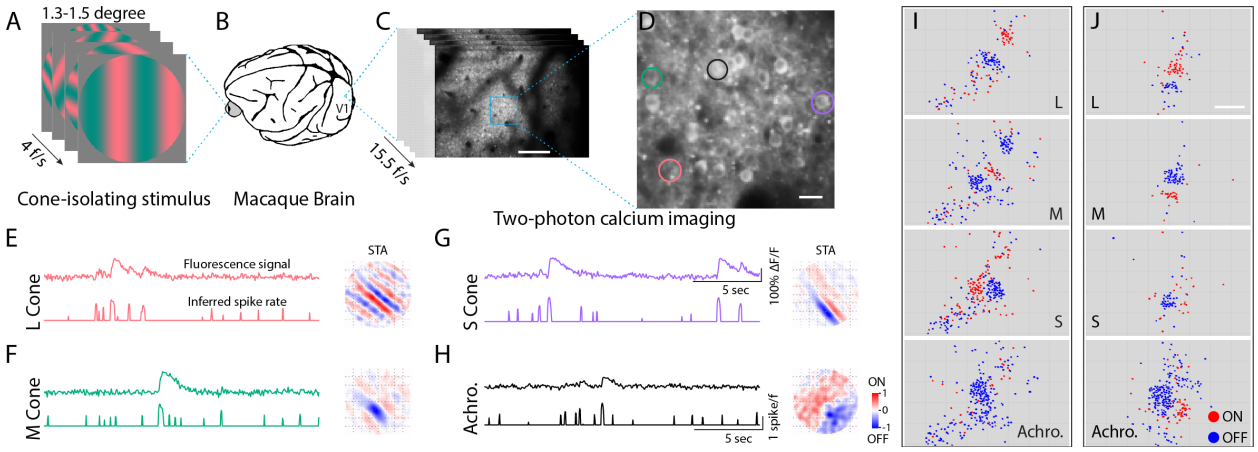

Fig. 2. Clustering of neurons with ON/OFF-dominant receptive fields. (A to **C)** Presentation of Hartley flashed gratings (A, L-cone isolating is shown as an example, 4 frames per second) to the anesthetized macaque monkey during simultaneous two-photon calcium imaging (C) in primary visual cortex (V1, B). Scale bar in (C) 200 µm. **(D** to **H)** Higher magnification view of the imaging region (D, scale bar: 20 µm) with four neurons selected as examples to show their fluorescence signals, inferred spike rates, and their receptive fields computed from spike-triggered average (STA) shown in (E to H). The color of traces in (E to H) are matched with the color of circles in (D) to indicate the origin of the signals. Responses to L-cone isolating (E), M-cone isolating (F), S-cone isolating (S), and achromatic (H) Hartley flash gratings are shown as four panels. The fluorescence signal (upper trace in each panel) is normalized to the response to blank condition ($\Delta F/F$). The spike rate (lower trace in each panel) is inferred from raw fluorescence signal (see materials and methods). Red colors in the STA images indicate ON sub-regions of spatial receptive fields, and blue indicates OFF sub-regions. Each grid in the STA images is 0.2 degree, and total size is 1.6 degree. **(I to J)** Functional maps of the locations of neurons with ON-dominant (red dots) and OFF-dominant (blue dots) receptive fields in response to each stimulus type (L, M, and S cone isolating and achromatic color (Achro.)). Neurons are organized in ON and OFF clusters. (I to J) are each from different imaging regions from animal A1 (more examples are shown in fig. S1); both illustrate two planes that were merged. Scale bar in (J): 200 µm; applies to all panels in (I) and (J).

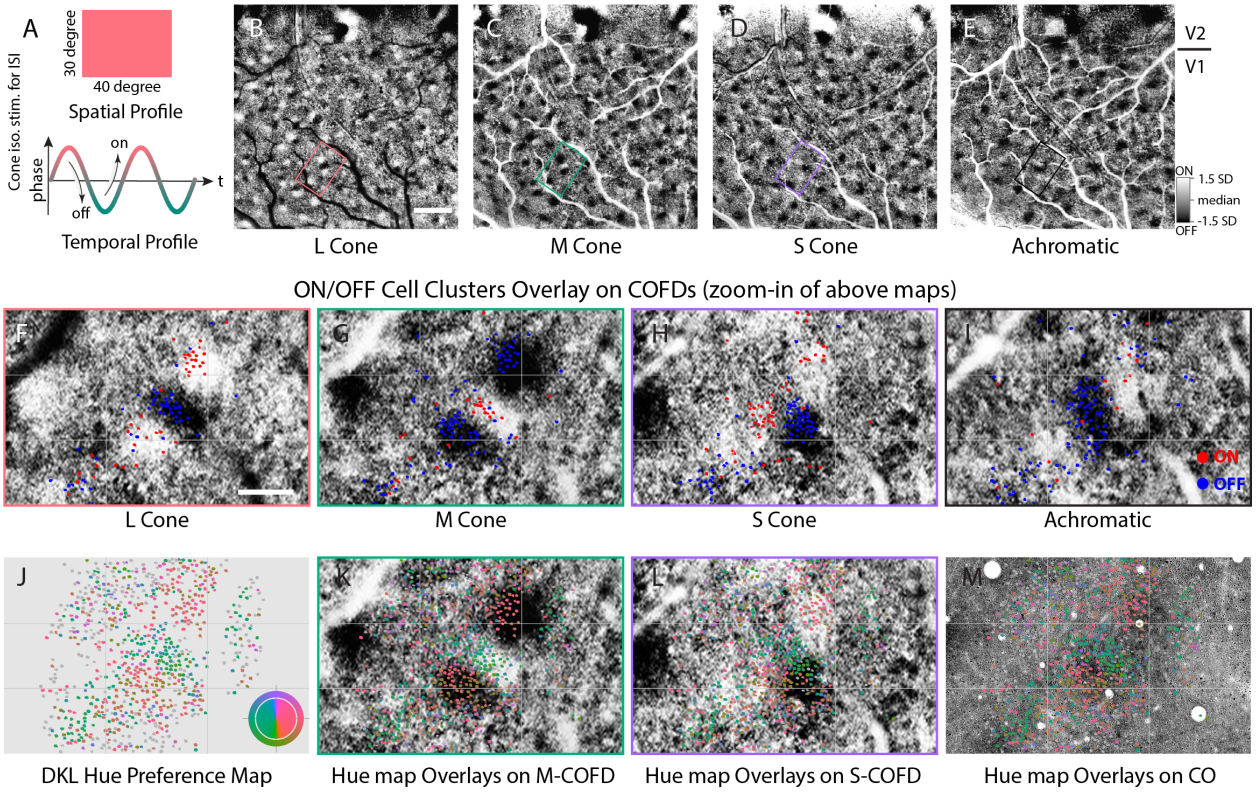

Fig. 3. COFDs obtained from ISI are aligned with ON and OFF clusters from 2PCI. (A) Continuous periodic full-field cone-isolating and achromatic stimuli (top) with corresponding sinusoidal temporal modulation (bottom, L-cone isolating stimulus is shown). **(B** to **E)** ISI phase maps reveal ON and OFF functional domains resulting from L-, M-, S-cone isolating and achromatic stimuli, respectively. Scale bar: 1mm. **(F** to **I)** 2PCI responses of neurons (colored dots) to L-, M-, and S-cone isolating and achromatic stimuli superimposed on corresponding aligned zoomed-in ISI phase maps from regions outlined in B to E. Individual neurons imaged with 2PCI depicted based on whether STA receptive field was predominantly ON (red) or OFF (blue). **(J)** DKL hue preference map from the same imaging region as shown in (F to I). Individual neurons are depicted based on the DKL hue to which they responded most strongly. Neurons that were not hue selective are plotted in grey. The inserted color key indicates the relationship between the hues for plotting the map (outer ring, DKL hues have maximal contrast that can be generated by our CRT monitor) and the hues used for stimulation (inner disk, DKL hues have matched cone-increment). **(K** to **M)** Same as J, overlaid on top of ISI M-cone, S-cone COFDs and cytochrome oxidase (CO) histology. Scale bar in (F): 200 µm; applies to (F) to (M). Note that grids were added in (F to M) for comparison purpose.

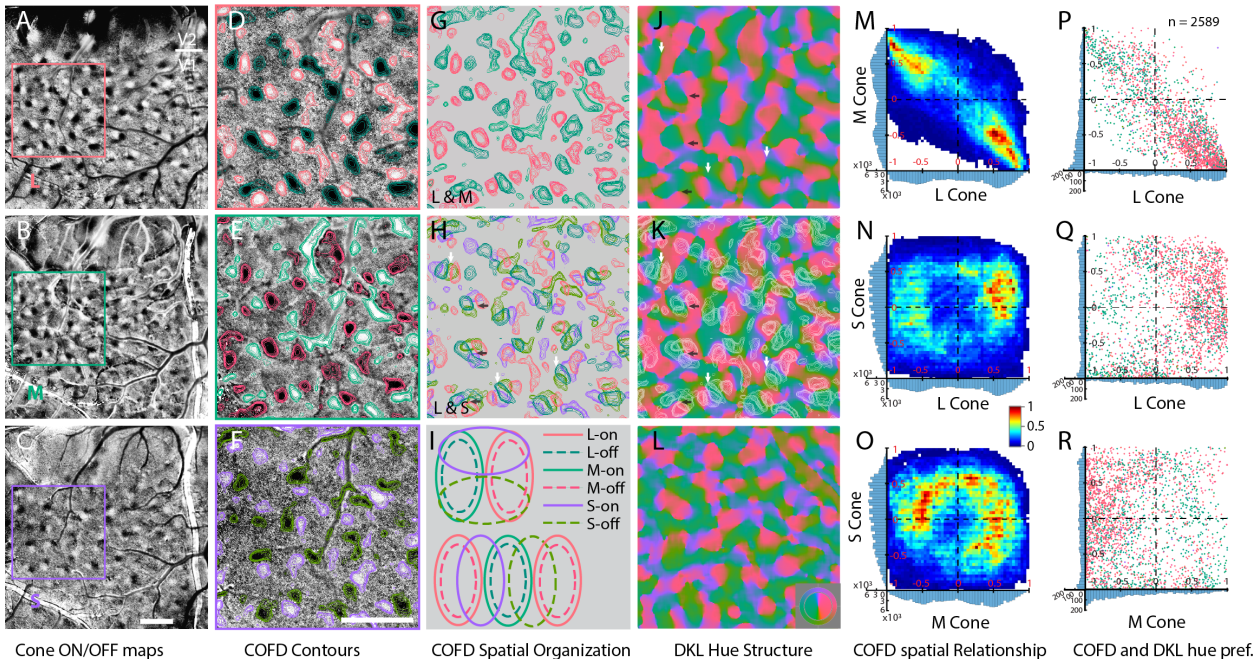

Fig. 4. Spatial relationships between COFDs and hue tuning from ISI and 2PCI. (A to **C)** COFDs from ISI phase maps in response to full-field periodic L-, M-, and S-cone isolating stimuli, respectively. Scale bar in (C): 1 mm; applies to (A to C). **(D** to **F)** Zoomed-in views of maps in A to C. Color contours for ON and OFF phases are overlaid on images based on ISI pixel values. Scale bar in (F): 1 mm; applies to (D to H) and (J to L). **(G** and **H)** Overlays of L-COFD contours (from D) with M-COFD contours (from E) (G) and L-COFDs with S-COFDs (from F) (H) to demonstrate spatial relationships between COFDs. Same scale as D to F. Additional examples are shown in fig. S3. L- and M-COFDs overlap extensively with have an anti-phase relationship; L-on COFDs align with M-off COFDs, and L-off align with M-on (G). In contrast, S-on and S-off COFDs tend to fall between and partially overlap with L+M- and M+L- COFDs (also see N and O) with a cross-overlap organization. (**I**) Schematic diagrams of the COFD relationships often seen in H. L+M-/M+L- pairs are often grouped with an S+/S-pair such that the pairs have orthogonal axes (H, dark arrows, schematized at top of I). Alternatively the pairs are arranged in parallel with S+ and S- COFDs interdigitating between L+M- and M+L- COFDs (H, white arrows, schematized at bottom of I). **(J** to **L)** DKL hue angle maps demonstrating pinwheel and parallel functional structures. Maps are generated from DKL hue-phase maps (e.g. Fig. 5). J and L are from different animals (A2 and A1, respectively), while K is same as J but with COFD contours superimposed. Same scale as D to F. Arrows in J and K are at the same locations as in H and illustrate the relationships between hue functional structures and COFDs. **(M** to **O)** 2D histograms of the spatial relationship between L, M, and S COFDs. The 1D histograms on the *x* and *y* axes display the number of pixels in each category. (Additional cases are shown in fig. S3). The anti-phase relationships between L and M COFDs are apparent in M, while interactions between L or M with S-COFDs have more balanced interactions across all phases (N, O). **(P** to **R)** Relationships between ISI COFD organization and DKL hue preference of individual neurons identified with 2PCI. Scatter plots are shown of mean normalized ISI cone-isolating phase map pixel values for pixels aligned to the location of each 2PCI imaged neuron. Histograms on *x* and *y* axes demonstrate the number of neurons with ISI pixel values in each bin. Individual neurons are colored according to their preferred DKL hue.

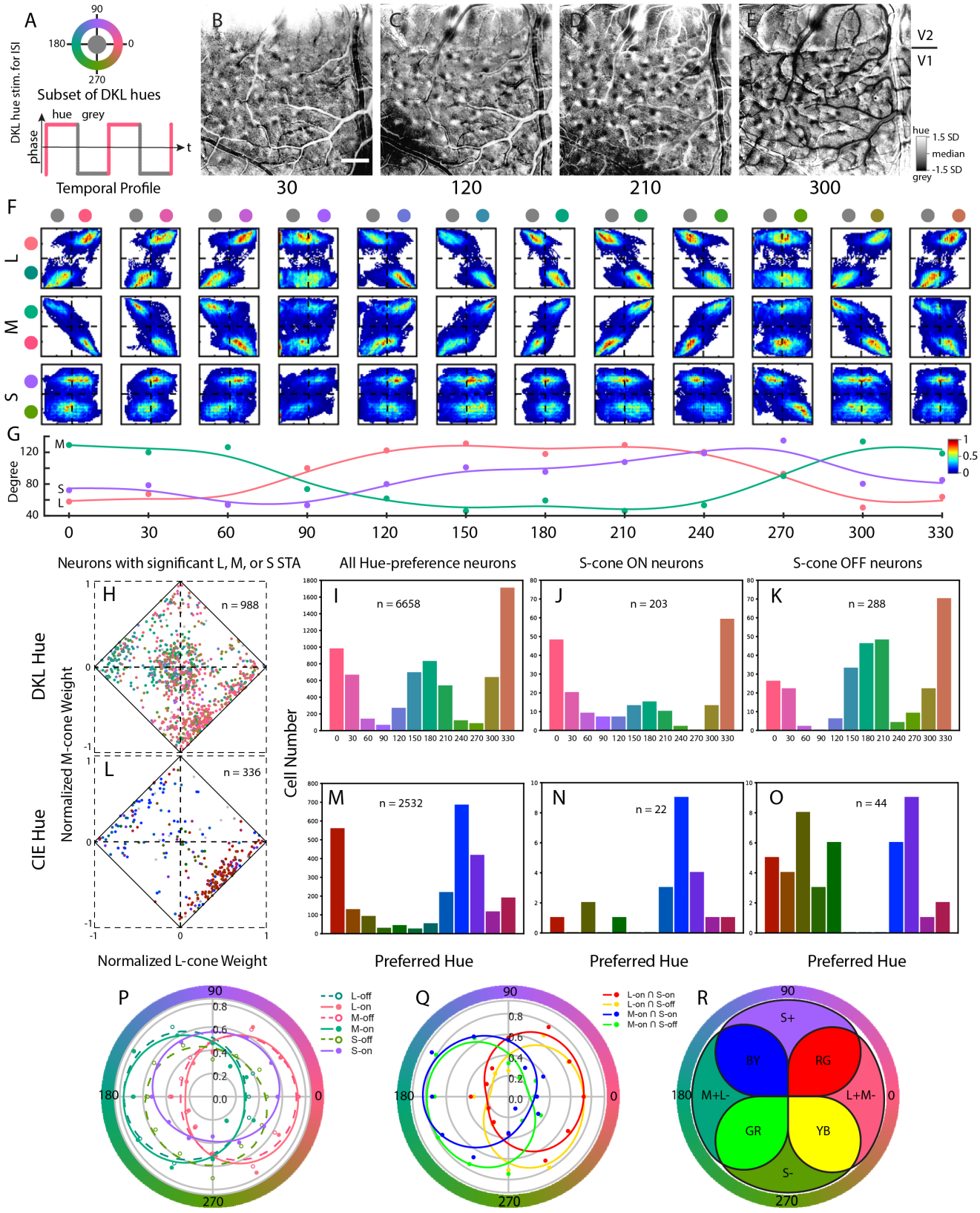

Fig. 5. Relationships between hue preference maps and COFDs. (A) Schematic of stimulus presentation. During ISI, twelve evenly spaced DKL hues were presented as full-field, square wave temporally modulated stimuli on a grey background (see materials and methods). L+/M-, L-/M+, S+, and S- directions correspond to 0, 180, 90, and 270 degree hue directions, respectively. **(B** to **E)** ISI phase maps in response to 30, 120, 210, and 300 degree hue directions (animal A2, other maps and another case, A1, are shown in fig. S4A). Maps have hue/grey phase pairs similar to ON/OFF phase pairs in COFD maps, but each with unique spatial

arrangements. Scale bar in (B): 1 mm; applies to (B to E). **(F** and **G)** Quantitative analyses of the spatial relationship between DKL hue preference domains and each type of COFD (another case, A1, is shown in Fig S4, B and C). Rows in F correspond to comparisons of hue maps with L (top row), M (middle row), and S (bottom row) COFDs. Columns in F and G correspond to relationships to hue-phase maps generated with stimuli modulated in the color directions indicated at bottom of G. **(F)** The ON and OFF phases of cone-isolating (L, M, and S) stimuli are shown as ON and OFF colors of each cone type on the left side. The colors of twelve DKL hues and grey are shown as color disks on the top of the panel. The bivariate histograms show systematic relationship between phase magnitude and signs for ISI pixels from COFDs and DKL hue preference domains. **(G)** The angles defined by the top 10% of pixel densities in each bivariate histogram for each cone type and in relation to each color direction are plotted. X-axis is the stimulus hue angle in DKL isoluminant plane, Y-axis is the pixel density angle calculated from each bivariate histogram (see materials and methods). Note that the L-cone and M-cone fitted curves have a counter-phase relationship, 180 degrees apart. The phase of the S-cone fitted curve is 90 degrees from and halfway between the L and M curves. (**H)** Comparisons for individual 2PCI neurons of the relationships between DKL hue preferences and cone input weights. 988 neurons with significant L, M, or S-cone STA kernels from 5 imaging regions (10 planes, see fig. S2) of A1 were selected to calculate normalized cone weights. L and M cone weights are plotted on the *x* and *y* axes in the diamond plot. Due to normalization summing total absolute values of weights to 1, S-cone weights are implicit as the distance from the edges of the diamond. Each neuron in the plot is colored according to its preferred DKL hue. Neurons with significant STAs, but which are not hue selective, are plotted as grey. **(I** to **K)** The distribution of preferred DKL hues of all hue-selective neurons (I), hue-selective neurons with significant S-ON STA (J), and hue-selective neurons with significant S-OFF STA (K). The preferred hue is shown as the color of bar, and the number of neurons sampled is shown in each panel. (Five imaging regions, 10 planes, from A1.) (**L** to **O**) Similar to H-K but using 2PCI data from cases in which CIE hues were presented. (L) 336 neurons with significant STA kernels from 4 imaging regions (3 from A3 and 1 from A4, 6 planes total) are plotted. (**P**) Hue tuning curves calculated from the means of ISI pixel values within each COFD region in response to each DKL hue direction. (**Q**) The hue tuning curves calculated from the means of ISI pixel values within each COFD-intersection region in response to each DKL hue direction. Method of curve fitting used in (P) and (Q) is described in materials and methods. Another case is shown in fig. S4, D and E. (**R**) Model of how cone-opponent mixing, facilitated by the spatial organization and overlap of COFDs creates color tuning and follows stage 3 mixing rules for color opponency and color appearance mechanisms. The organization allows four intersections between L/M and S/(L+M) cone-opponent mechanisms at the four overlapping regions of COFDs. This mixing generates opponent color mechanisms and encompasses the four "unique colors" (red – RG; green – GR; yellow – YB; blue – BY).

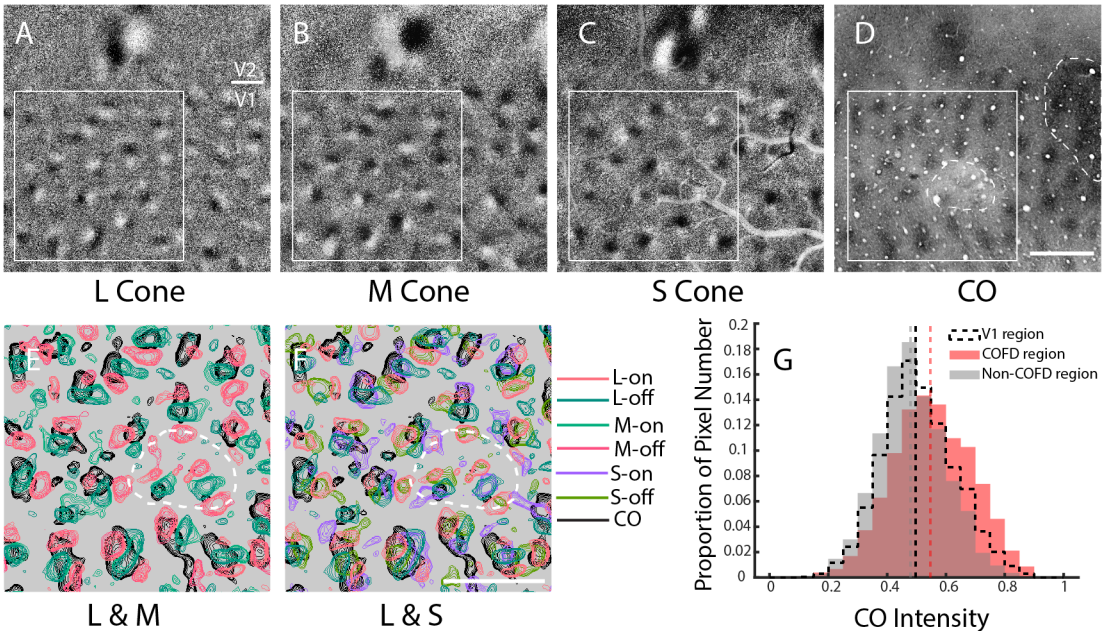

Fig. 6. Spatial relationship between COFDs and CO blobs. (**A** to **C**) L- (A), M- (B), and S-cone (C) COFD maps of V1 and V2 from animal A5. (**D**) Aligned image of CO staining from the same region as (A to C). Scale bar in (D): 1 mm; applies to (A to D). (**E** and **F**) Slightly higher-power view of the COFD and CO contours from the region within the white square shown in (A to D). More cases are shown in fig. 5S. Scale bar in (F): 1 mm; applies to (E) and (F). (**G**) Histogram of CO intensity distributions in COFD, non-COFD and whole V1 regions. Dash lines are median of the distribution in each region. The CO intensity distribution in COFD regions is significantly higher than that in non-COFD regions (n = 96 COFD regions, P = 0.0062, Wilcoxon signed rank test, see materials and methods). Note that dotted white outline in (D to F) indicates region restricted from quantitative analysis due to damage by an electrode penetration (subsequent to ISI data collection) and loss of CO staining.